Green synthesis of Ag nanoparticles using elm pod polysaccharide for catalysis and bacteriostasis

Mengmeng He[a], Zengsheng Han[a,b], Ying Liang[a], Han Zhao[a], Xianbing Ji[c], Guanglong Ma[d], Yanshuai Cui[c], Longgang Wang[a,b]**

a. *Key Laboratory of Applied Chemistry, Nano-biotechnology Key Lab of Hebei Province, Hebei Key Laboratory of Heavy Metal Deep-Remediation in Water and Resource Reuse, College of Environmental and Chemical Engineering, Yanshan University, Qinhuangdao, 066004, China*

b. *State Key Laboratory of Metastable Materials Science and Technology, Yanshan University, Qinhuangdao, 066004, China*

c. *Hebei University of Environmental Engineering, Qinhuangdao, 066102, China*

d. *Centre for cancer immunology, Faculty of medicine, University of Southampton, Southampton, SO166YD, UK*

* *Corresponding author:* Zengsheng Han, Longgang Wang

Abstract

The green synthesis of silver nanoparticles (Ag NPs) for catalysis and biological applications has gained great interest. Natural elm pods are a type of food that possesses anti-inflammatory and pain-relieving effects. In this study, elm pod polysaccharide (EPP) was extracted from elm pods using hot water extraction for the first time. Biocompatible EPP-stabilized silver nanoparticles (EPP-Ag_n NPs) were prepared by using a green synthesis method. The EPP-Ag_{25} NPs had a hydrodynamic size of 40.9 nm and a highly negative surface charge of -27.4 mV. Furthermore, EPP-Ag_{25} NPs exhibited high catalytic activity for the reduction of 4-nitrophenol, and the catalytic reaction followed a pseudo-first order kinetic equation. More importantly, the inhibition rate of EPP-Ag_{25} NPs on *Escherichia coli* was 71% when samples were treated with an 808 nm laser. Besides, EPP-Ag_n NPs effectively inhibited the proliferation of tumor cells irradiated by an 808 nm laser. The improved performance of EPP-Ag_n NPs was due to the good stability of EPP. Taken together, EPP-Ag_n NPs had good stability, catalytic activity, antibacterial and antitumor ability under laser irradiation. EPP is a good stabilizer for many nanoparticles which have broad applications in the field of catalysis and biomedicine in the future.

Key words: elm pod polysaccharide; silver nanoparticles; catalysis

1. Introduction

People pay more attention to environmental issues with the development of industry and society. Organic compounds in wastewater are toxic to humans. 4-Nitrophenol (4-NP) is one of the most toxic pollutants. 4-NP can cause serious health problems such as chest pain, headache, and vomitus. Therefore, it is very important to remove 4-NP or convert it into 4-aminophenol (4-AP), which has good functions and low toxicity. In addition, antibiotic misuse has resulted in the emergence and spread of multi-drug resistant bacteria in the world. New antibacterial agents have been developed with the goal of improving antibacterial activity, lowering toxicity, and making preparation easier [1].

Noble metal nanoparticles are playing an increasingly important role in the catalytic degradation of organic waste, or biomedicine as antibacterial agents and antitumor agents [2-4]. Silver nanoparticles (Ag NPs) in noble metal nanoparticle have the advantages of low cost, low toxicity, strong antibacterial ability, and easy preparation [5]. Ag NPs have been used in the catalysis of organic pollutants such as 4-NP, as well as for antibacterial and photothermal effects [6-8]. Because of the high surface energy of noble metal nanoparticles, bare silver nanoparticles are unstable in solution and prone to aggregation. The aggregation of metal nanoparticles often results in their precipitation and decreased performance [9-12]. When Ag NPs agglomerate, their catalytic activity is significantly reduced [13]. Furthermore, poor stability reduces the surface plasmon resonance (SPR) capability and photothermal performance of Ag NPs [14]. Stabilizers including organic ligands, linear polymers, and dendrimers have been widely used to improve the stability of Ag NPs [15]. Manjari Gangarapu and his colleagues reported dendrimer-encapsulated Ag NPs for catalytic oxidation [16]. Green and biocompatible stabilizers have attracted a great attention among stabilizers [17, 18].

The green method, which employs various plant extracts, has many advantages such as environmental protection and low cost [19, 20]. These plant extracts include ginkgo biloba extract [21, 22], pomegranate extract [3], jujube extract [23], and shiitake mushroom extract. The antioxidant activity of plant extracts is mainly due to flavonoids,

polyphenols, and polysaccharide. However, these plant extracts contain a wide range of components, resulting in different reducing power and stabilizing ability. Therefore, it may be difficult to precisely control the size and morphology of metal nanoparticles. Eco-friendly natural polysaccharides with high molecular weight have plenty of hydroxyl groups, proving their ability as stabilizing and capping agents [24]. Different polysaccharides have different molecular weights, solubility, and reducing ability, all of which influence the formation and stability of metal nanoparticles. The seed of the elm tree is the elm pod. The elm pod reduces the body's anger, inflammation, swelling, pain, cough, and phlegm. The elm pod polysaccharide (EPP), as a new polysaccharide extracted from elm pod, is likely to have reducibility and stability. Therefore, the EPP may be a good stabilizer for the Ag NPs.

Herein, EPP was extracted from the elm pod by using hot water extraction for the first time. Elm pod polysaccharide stabilized silver nanoparticles (EPP-Ag_n NPs) with good biocompatibility and stability were prepared using EPP as a stabilizer for the first time. EPP-Ag_n NPs were used to catalyze the degradation of organic pollutants 4-NP. In addition, EPP-Ag_{25} NPs showed a photothermal effect when they were exposed to 808 nm near-infrared light. Because of the synergistic effect of Ag NPs and heat generation by near-infrared light, EPP-Ag_{25} NPs had an enhanced antibacterial effect on *Escherichia coli*. The MTT assay revealed that EPP-Ag_n NPs had good biocompatibility; however, the toxicity was increased when they were exposed to an 808 nm laser. Therefore, EPP-Ag_n NPs not only demonstrated good catalytic ability in the treatment of organic waste, but also revealed photothermal antibacterial and antitumor effects when they were exposed to laser irradiation.

2. Materials and methods

2.1. Materials

Materials were represented in the Supplementary Material.

2.2. Preparation of EPP-Ag_n NPs

The EPP was extracted by hydrothermal method. Elm pods were washed, dried and ground into powder. The elm pod powder (20 g) was mixed with deionized water at a

ratio of 1:25. The extracted solution was degreased with ethanol (50 mL), removed protein with Sevage method, and decolorized with hydrogen peroxide (30 mL). The organic reagents added in the above-mentioned steps were removed by rotary evaporation, and some small molecular impurities were removed by dialysis. The final solution was freeze-dried to obtain EPP powder. The yield was 5%.

1 mL of EPP (1 mg/mL) and $AgNO_3$ (8 mM) were mixed in a 2 mL PE tube. The molar ratios of EPP to $AgNO_3$ were 1:10, 1:25, and 1:40, respectively. The mixed solution was placed in a Thermo Shaker set to 60°C and 600 rpm for 10 min. The mixed solution was then treated with an excess of ascorbic acid (1 mg/mL). The color of the solution changed from colorless to brown after 3 h. The solutions were dialyzed for 24 h to produce EPP-Ag_n NPs (n = 10, 25, 40), then they were stored at 4°C.

To study the role the EPP, the reduction of $AgNO_3$ by ascorbic acid yielded `Ag NPs-3 without using EPP. The addition amount and experimental steps were the same as the preparation of EPP-Ag_{25} NPs.

1 mL of EPP (1 mg/mL) and $AgNO_3$ (8 mM) were mixed in a 2 mL PE tube. The molar ratio of EPP to $AgNO_3$ was 1:25. The mixed solution was placed in a Thermo Shaker set to 60°C and 600 rpm for 12 h. The solutions were dialyzed for 24 h to yield the final products EPP-Ag_{25} NPs-12, which were then stored at 4°C.

2.3. Characterization

EPP-Ag_n NPs were monitored by the UV-Vis spectrophotometer (TU1810PC). The functional groups of EPP and EPP-Ag_n NPs were determined by FTIR (E55-FRA106). The nuclear magnetic resonance of EPP was studied by Bruker AVANCE III 600. The size and morphology of EPP-Ag_n NPs were observed by TEM (HT 7700). The XPS of EPP-Ag_n NPs was determined using a Thermo SCIENTIFIC ESCALAB 250Xi. The hydrodynamic size and zeta potential of EPP-Ag_n NPs were determined by DLS (Zetasizer Nano-ZS90).

2.4. Catalytic performance

The catalytic reduction of 4-NP experimental process consisted of three parts.

(1) The UV-Vis spectra of (I) 4-NP (2 mL, 0.6 mM) and (II) 4-NP (200 μL, 0.6 mM),

deionized water (800 μL) and freshly prepared $NaBH_4$ (1 mL, 0.5 M) were measured.

(2) Time-dependent reduction of 4-NP: 4-NP (200 μL, 0.6 mM), deionized water (800 μL) and EPP-Ag_{25} NPs (50 μL, C_{Ag} = 0.013 mM) were added to the quartz cuvette, freshly prepared $NaBH_4$ (1 mL, 0.5 M) was added to mixed solution, and UV-Vis spectra were measured every 2 min.

(3) Concentration-dependent experiment of 4-NP catalysis: 4-NP (200 μL, 0.6 mM) and different amounts of EPP-Ag_{25} NPs (50, 100, 150 μL) were mixed and the volume was adjusted to 1 mL by adding deionized water. Freshly prepared $NaBH_4$ was added to above mixed solution. The effect of different concentrations of EPP-Ag_{25} NPs on their catalytic ability was measured by a spectrophotometer.

2.5. Photothermal effects evaluation

1 mL of samples (EPP-Ag_{25} NPs, Ag NPs-3, EPP, and water) were exposed to an 808 nm near-infrared laser with a power of 1.75 W/cm^2 for 10 min. Furthermore, the EPP-Ag_{25} NPs solution was continuously irradiated by an 808 nm near-infrared laser with a power of 1.75 W/cm^2. When the temperature of solution was the highest, the solution of EPP-Ag_{25} NPs was naturally cooled to room temperature. Finally, the temperature of the EPP-Ag_{25} NPs solution was detected to rise and fall 5 times in order to determine the photothermal stability of EPP-Ag_{25} NPs.

2.6. Antibacterial performance

The antibacterial property of EPP-Ag_{25} NPs was measured in a 96-well bacterial culture plate. 120 μL of bacterial solution was added in a 96-well plate, and 30 μL of samples (C_{Ag} = 100-500 μg/mL) such as EPP, Ag NPs-3, EPP-Ag_{25} NPs were added in the bacterial solution. Afterwards, the 96-well plate was placed on a constant temperature shaker at 37°C for 4 h. EPP-Ag_{25} NPs + L group means that EPP-Ag_{25} NPs were incubated on *Escherichia coli* and irradiated with an 808 nm near-infrared laser (1.75 W/cm^2) for 10 min. Finally, the absorbance was measured at 600 nm to determine the antibacterial performance of EPP-Ag_{25} NPs. The inhibition rate was calculated by formula (1):

$$\text{Inhibition rate} = (1 - \frac{A_{samples}}{A_{control\ group}}) \times 100\% \quad (1)$$

2.7. Cell viability assay

The MTT method was used to detect the effect of EPP-Ag_n NPs on cell viability [25]. HeLa cells were seeded into 96-well tissue culture plates (1×10^4 cells/well). After 24 h, samples ($C_{samples}$ = 5-100 μg/mL) such as EPP, $AgNO_3$, EPP-Ag_n NPs were added to the 96-well tissue culture plates and incubated for 12 h. After that, the EPP+L group was irradiated with 808 nm near-infrared laser for 10 min per hole after 8 h. Then, MTT (100 μL, 500 μg/mL) was added. After 4 h, the MTT solution was taken out, and 150 μL of DMSO was added to dissolve the formazan. The absorbance was detected at 490 nm after 10 min. Cell viability was calculated as formula (2):

$$\text{Cell viability} = \frac{A_{samples}}{A_{control\ group}} \times 100\% \quad (2)$$

3. Results and discussion

3.1. Characterization of EPP

Elm pods are the seeds of the elm tree, and they are rich in proteins, vitamins, and minerals. The elm pod reduces the body's anger, inflammation, sterilization, swelling, pain, and cough. Herein, EPP was extracted from the elm pod. The relative molecular weight of EPP was determined by gel permeation chromatography (GPC). **Fig. S1** shows that the number average molecular weight of EPP was 10800 Da based on the elution curve. The protein content of EPP was 90% based on standard curve of protein content, which indicated a good purity of extracted EPP. In addition, the reducing ability of polysaccharide results in the reduction of Fe^{3+} in $K_3[Fe(CN)_6]$ to Fe^{2+} in $K_4Fe(CN)_6$, $K_4Fe(CN)_6$ and $FeCl_3$ further react to produce $Fe_4[Fe(CN)_6]_3$ with the highest absorption peak at 700 nm [26]. As shown in **Fig. 1a**, the absorbance of EPP was 0.216 with the concentration of EPP for 2 mg/mL, proving that EPP had the potential ability to reduce Ag^+ to Ag. Besides, the molecular structure of EPP was analyzed by ^1H NMR spectrum. As shown in **Fig. 1b**, a large number of signals appeared in the 1.0-3.0 ppm region, which meant that EPP may contain a large number of saturated hydrocarbon groups. The proton signal that appeared in the range of 3.5-5.5 ppm may belong to the

-OH in the EPP. Proton signals from 4.9 ppm to 6.3 ppm presumably were ascribed to α-type glycosidic bonds.

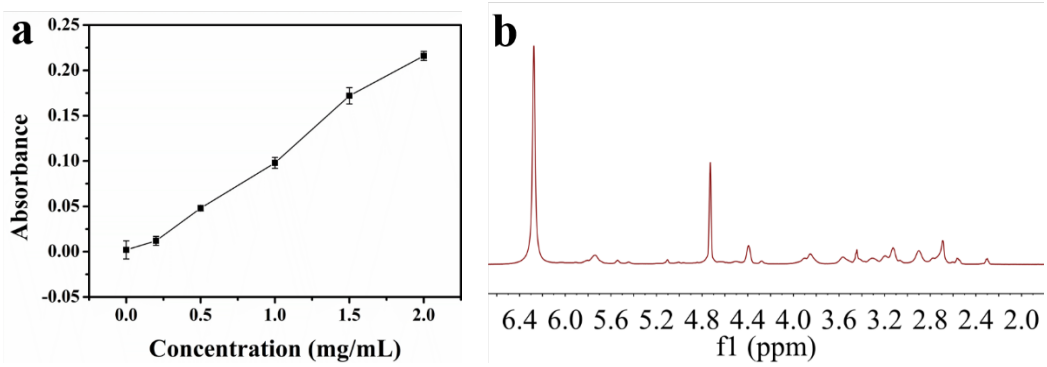

Fig. 1. (a) Reducing power of EPP and (b) ^{1}H-NMR spectrum of EPP

3.2. Characterization of EPP-Ag$_n$ NPs

EPP and $AgNO_3$ were incubated in a Thermo Shaker for 10 min, excess ascorbic acid was added and they were incubated for 3 h. EPP was a stabilizer and ascorbic acid was a reducing agent in this reaction. The formation of EPP-Ag$_n$ NPs was judged by using UV-Vis spectroscopy. As shown in **Fig. 2a**, EPP and $AgNO_3$ solutions had no absorption peak at 430 nm, while a new absorption peak was detected at 430 nm for EPP-Ag$_n$ NPs after reaction. The absorption peak of EPP-Ag$_n$ NPs at 430 nm indicated that EPP-Ag$_n$ NPs were formed. In addition, **Fig. 2b** shows that the color of EPP-Ag$_n$ NPs solution was brown, which was similar to the color of Ag NPs in previous report [27]. Therefore, these results proved that EPP-Ag$_n$ NPs were successfully prepared. EPP-Ag$_n$ NPs were stable in solution for two weeks without precipitation observing by naked eyes. Besides, EPP and $AgNO_3$ (n_{EPP}: n_{AgNO3} = 1:25) reacted in a Thermo Shaker set to 60°C and 600 rpm for 12 h to get EPP-Ag$_{25}$ NPs-12 solution without precipitation. As shown in **Fig. S2a**, EPP solution and $AgNO_3$ solutions had no absorption peak at 430 nm, while a new absorption peak was detected at 430 nm for EPP-Ag$_{25}$ NPs-12, which indicated that Ag NPs formed inside of EPP-Ag$_{25}$ NPs-12. **Fig. S2b** shows that the color of EPP-Ag$_{25}$ NPs-12 solution was yellow without precipitation, suggesting the stabilizing and reducing ability of EPP. Silver nitrate was reduced by ascorbic acid without adding EPP to form Ag NPs-3. Ag NPs-3 showed aggregated and precipitated state after several hours in **Fig. S3**. Through the comparison of the three methods, it can be concluded that

EPP acted as a stabilizer and weak reducing agent.

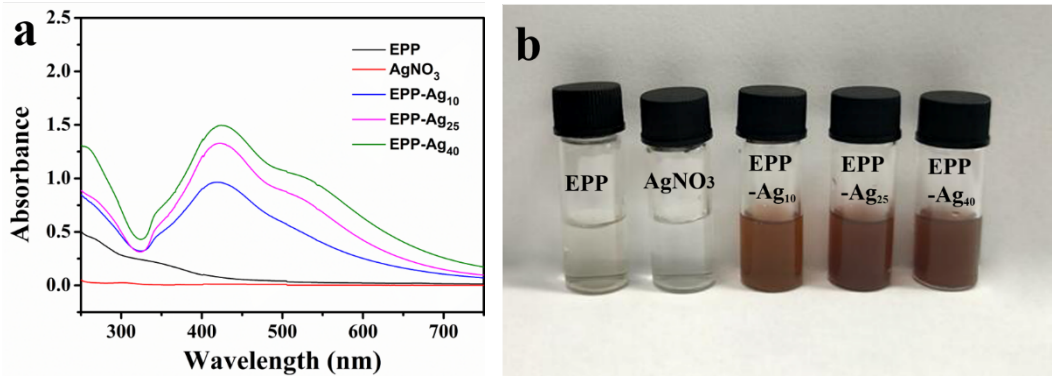

Fig. 2. (a) UV-Vis spectra and (b) corresponding photographs of EPP, $AgNO_3$, EPP-Ag_n NPs (n = 10, 25, 40), respectively

The solution of EPP-Ag_n NPs was dropped on the grid of carbon membrane, the size and distribution of Ag NPs in EPP-Ag_n NPs were measured by TEM. As shown in **Fig. 3 (a, b, c)**, the TEM images show that most of Ag NPs in EPP-Ag_n NPs were nearly spherical, and some Ag NPs were triangular and rod-shaped. The dispersion state of EPP-Ag_n NPs was well, which may be related to the EPP template. As shown in **Fig. 3 (d, e, f)**, the sizes of Ag NPs inside EPP-Ag_{10} NPs, EPP-Ag_{25} NPs and EPP-Ag_{40} NPs were 22.5 ± 8.6, 24.2 ± 8.0 and 30.0 ± 11.5 nm, respectively. Therefore, EPP-Ag_n NPs with Ag NPs from 22.5 to 30.0 nm were successfully prepared. As shown in **Fig. S4,** the TEM image shows that the Ag NPs-3 directly synthesized from silver nitrate and ascorbic acid without EPP are in an aggregated state. It can be seen that EPP plays a stabilizing role.

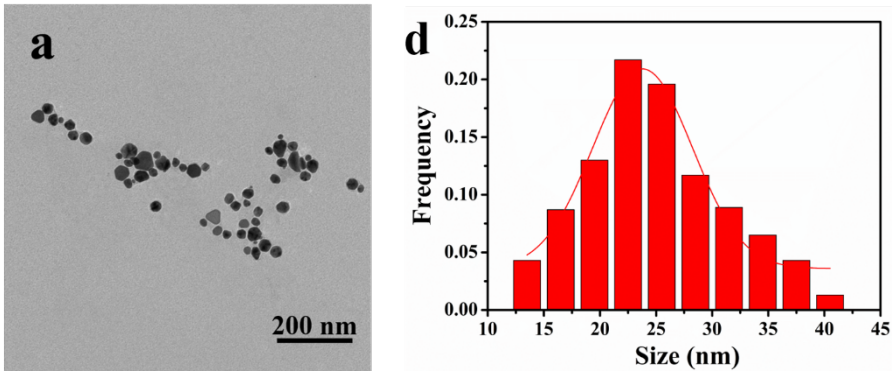

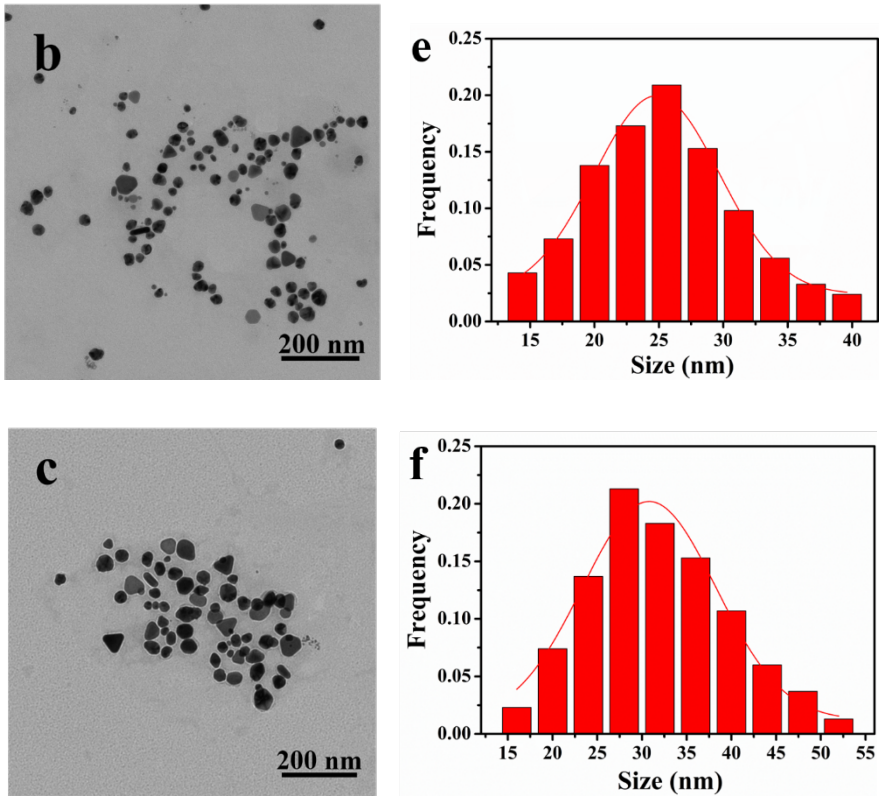

Fig. 3. TEM image of (a) EPP-Ag_{10} NPs, (b) EPP-Ag_{25} NPs and (c) EPP-Ag_{40} NPs, size statistics of (d) EPP-Ag_{10} NPs, (e) EPP-Ag_{25} NPs and (f) EPP-Ag_{40} NPs

The hydrodynamic size and zeta potential of nanoparticles are relevant to their applications in catalysis and nanomedicine [28]. The hydrodynamic size and zeta potential of EPP-Ag_n NPs (n = 10, 25, 40) in water was tested by DLS. As shown in **Fig. 4a**, the hydrodynamic size of EPP was 30.7 nm, and EPP-Ag_{10} NPs, EPP-Ag_{25} NPs, and EPP-Ag_{40} NPs had a hydrodynamic size of 36.7, 40.9 and 46.4 nm, respectively. Thus, the hydrodynamic size of EPP-Ag_n NPs based on the DLS test was larger than that based on TEM result. This is because that water molecules were adsorbed around the EPP and EPP-Ag_n NPs in solution, and they were in a hydrated state. Besides, **Fig. 4b** shows that the zeta potential of EPP, EPP-Ag_{10} NPs, EPP-Ag_{25} NPs, and EPP-Ag_{40} NPs was -26.8, -23.6, -27.4 and -27.4 mV, respectively. Zeta potential was a parameter of stability of nanoparticles. The higher the absolute value of the zeta potential of nanoparticles was, and the better stability of the system was. The absolute value of zeta potential of EPP-Ag_n NPs was larger than 20 mV, which resulted in good stability of EPP-Ag_n NPs.

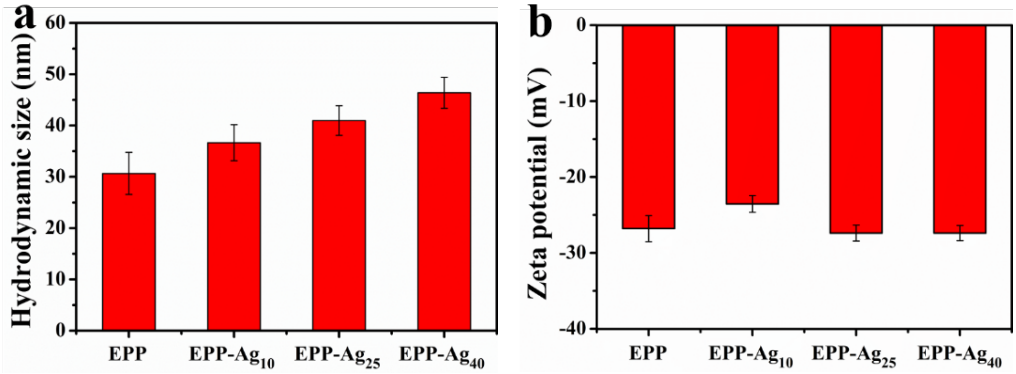

Fig. 4. (a) The hydrodynamic size and (b) zeta potential of EPP and EPP-Ag_n NPs in solution

The crystal form and spatial structure of EPP-Ag_{25} NPs were characterized by XRD [29]. As shown in **Fig. 5a**, there were five diffraction signals at 2θ at 38.116°, 44.277°, 64.426°, 77.472°, 81.536°, they matched (1 1 1), (2 0 0), (2 2 0), (3 1 1) and (2 2 2) planes, respectively. The XRD result indicated that EPP-Ag_{25} NPs had face-centered cubic (FCC) of Ag crystal planes. In order to analyze the elements and valence states of EPP-Ag_n NPs, Thermo SCIENTIFIC ESCALAB 250Xi was used to record the XPS spectrum of EPP-Ag_n NPs. It can be seen from **Fig. 5b** that the binding energy of C 1s and O 1s was 284.6 eV and 531.4 eV, respectively. C and O elements came from EPP, other Ag elements came from $AgNO_3$. **Fig. 5c** shows that the binding energy of Ag $3d_{3/2}$ and Ag $3d_{5/2}$ was 373.5 eV and 367.5 eV, respectively. Pratibha Attri and his colleagues report the binding energy of Ag NPs, Ag $3d_{3/2}$ and Ag $3d_{5/2}$ are 366 eV and 373 eV, respectively [30]. These results indicated successful preparation of EPP-Ag_{25} NPs.

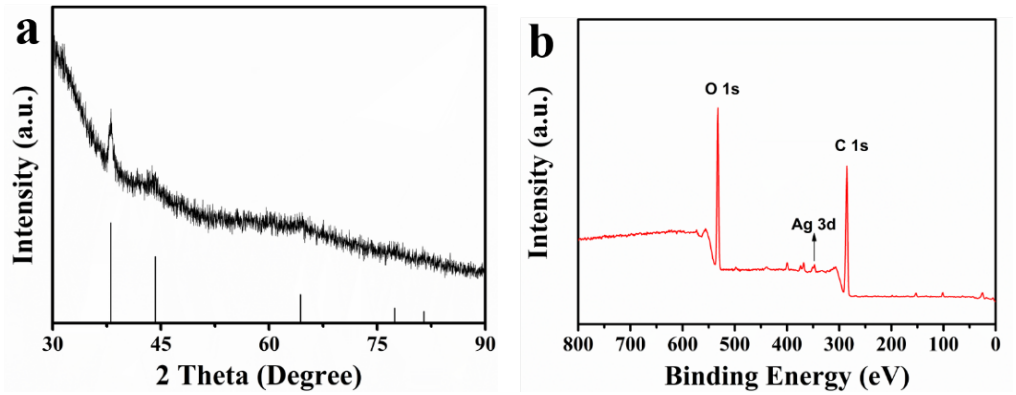

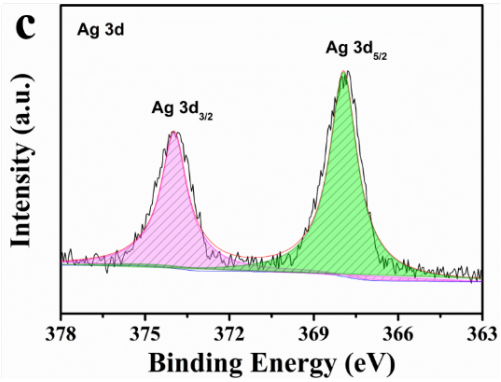

Fig. 5. (a) XRD spectrum, (b) XPS spectrum of EPP-Ag_{25} NPs and (c) high resolution XPS spectrum of Ag 3d

3.3. Catalytic activity

The catalytic performance of EPP-Ag_{25} NPs in the reduction of 4-NP [31] was evaluated. As shown in **Fig. 6a**, when $NaBH_4$ was added to 4-NP solution, 4-NP was converted to 4-nitro phenol ion, the absorption peak shifted from 317 nm to 400 nm [32]. As shown in **Fig. 6b**, the peak of 4-NP at 400 nm dropped rapidly and the peak of 4-AP at 300 nm increased after adding the EPP-Ag_{25} NPs catalyst, which indicated that 4-AP was generated. Since the concentration of $NaBH_4$ in the reaction system is much higher than that of 4-NP, the first-order kinetic model can be used to analyze the catalytic reduction process of 4-NP. The reaction rate constant k_{app} can be calculated using the following formula (3):

$$\ln\left(\frac{C_t}{C_0}\right) = \ln\left(\frac{A_t}{A_0}\right) = -k_{app}t \qquad (3)$$

According to formula (3), k_{app} is the reaction rate constant. The k_{app} of the catalyst EPP-Ag_{25} NPs for catalytic reduction of 4-NP was calculated. **Fig. 6c** shows that the relationship between ln (C_t/C_0) and time of EPP-Ag_{25} NPs was linear. Therefore, the catalytic reaction followed the first-order kinetic equation [33]. The k_{app} and TOF of EPP-Ag_{25} NPs were 9.90×10^{-3} s^{-1} and 771.62 h^{-1}, respectively. Normalized rate constant ($k_{nor} = \frac{k_{app}}{C_{Ag}}$) of EPP-$Ag_{25}$ NPs was 5.94 s^{-1} mM^{-1}. The performance of the catalyst was compared with previously reported nanoparticles and was epitomized in **Table 1**. It can be seen that the conversion rate of 4-NP reached 90% after 14 min in **Fig. 6d**. The conversion rate of 4-NP indicated that EPP-Ag_{25} NPs had good catalytic performance for the reduction of 4-NP. **Fig. 6e** shows the effect of EPP-Ag_{25} NPs at

different concentrations on the catalytic reduction of 4-NP. As shown in **Fig. 6f**, the k_{app} of the catalytic reaction gradually increased with increasing EPP-Ag_{25} NPs concentration.

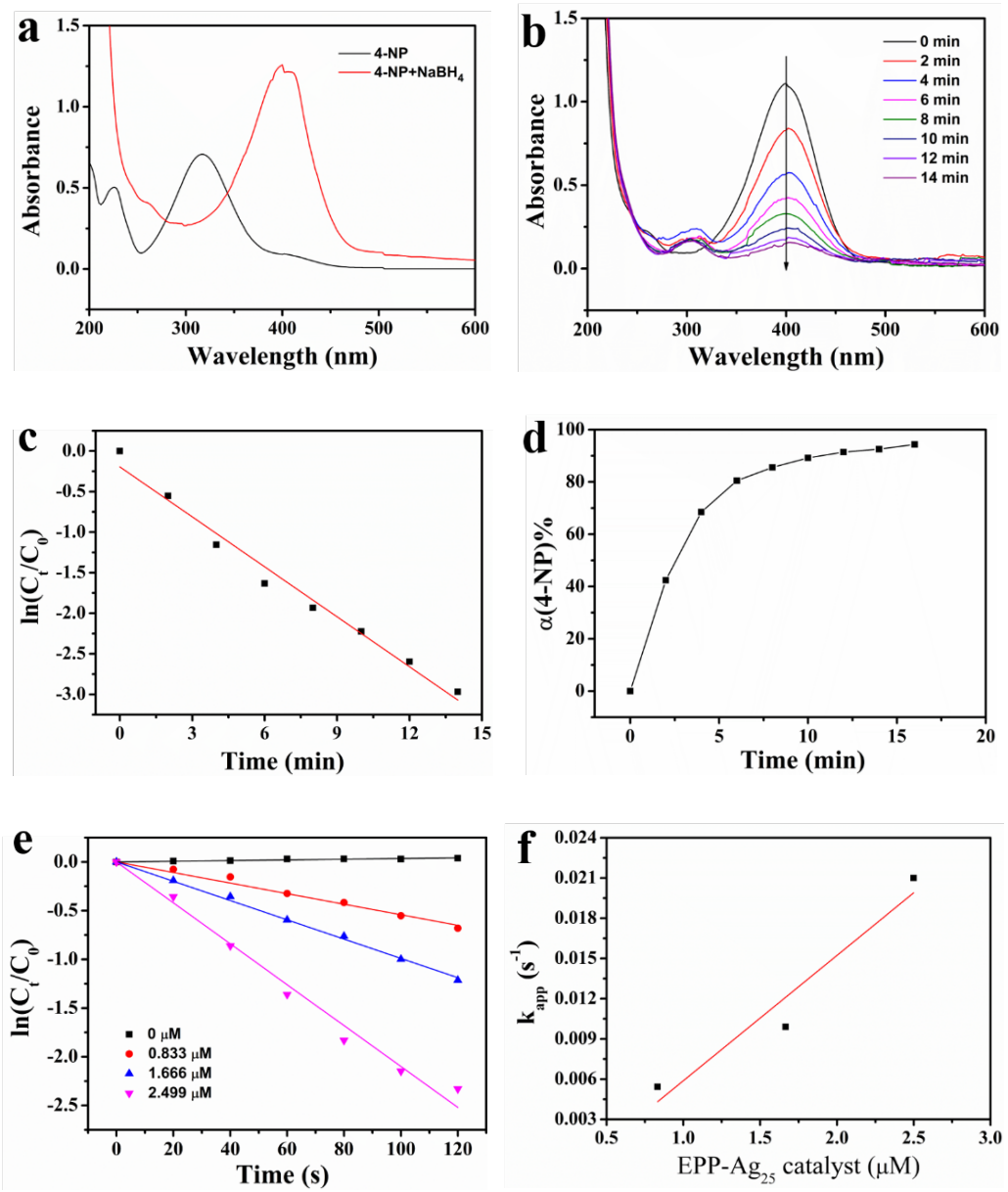

Fig. 6. (a) UV-Vis spectra of 4-NP and 4-NP + $NaBH_4$, (b) UV-Vis spectra of 4-NP + $NaBH_4$ after addition of EPP-Ag_{25} NPs every 2 min and corresponding (c) catalytic kinetics and (d) 4-NP conversion rate, (e) the relationship between ln (C_t /C_0) and the reaction time and (f) the relationship between k_{app} and concentration of EPP-Ag_{25} NPs

Table 1 Comparison of k_{app} and TOF of EPP-Ag_{25} NPs with other catalysts

Catalyst	Ag size (nm)	k_{app} ($\times 10^{-3}$ s^{-1})	TOF (h^{-1})	Ref.
EPP-Ag_{25} NPs	24.2±8.0	9.9	771.62	This work
Ag NPs	5.8±2.5	15.5	720	[34]
Ag NPs/Si NSs	2.7	80.19	211.2	[35]
Ag/GSH-rGO	3.57	9.16	-	[36]
Fe_3O_4@PS@Ag	-	8.6	-	[37]
Ag NPs	11.0±3.0	1.83	170	[38]
MCS-3	10	37.8	72.7	[39]
Ag NPs@NC	12.1	3.25	0.135	[40]

3.4. Photothermal performance

Proteins and DNA involved in cell survival and reproduction were easily destroyed in the environment of overheating (>43°C), leading to cell death under overheated conditions [41]. The 808 nm laser was selected because it has the advantages of good light penetration and little absorption in tissue cells [42]. The photothermal performance of EPP-Ag_{25} NPs was shown in **Fig. 7a**, the temperature of H_2O, EPP, Ag NPs-3 and EPP-Ag_{25} NPs raised from 24 to 26.8, 27.0, 35.1 and 43.5℃ within 600 s, respectively. In order to further calculate the photothermal conversion efficiency, the heating and cooling curves of EPP-Ag_{25} NPs were recorded. As shown in **Fig. 7b**, the photothermal conversion efficiency was 22%. This was due to the special three-dimensional structure of EPP-Ag_{25} NPs which included not only spherical structure but also triangular structures. The photothermal stability of EPP-Ag_n NPs was monitored for five cycles of irradiation. As shown in **Fig. 7c**, the maximum temperature of EPP-Ag_{25} NPs stably reached 48°C in five circles, indicating that EPP-Agn NPs had good stability of conversion ability. Ag NPs-3 showed aggregated and precipitated state after several hours. However, EPP-Ag_n NPs were stable in solution for two weeks without precipitation observing by naked eyes. Thus, the concentration of Ag NPs-3 in the upper liquid was much smaller than that of EPP-Ag_n NPs. Therefore, EPP-Ag_{25} NPs had better ability of absorbing near-infrared light and higher temperature rise than Ag NPs-3. The good stability of EPP-Ag_{25} NPs was due to the role of EPP acting as a stabilizer.

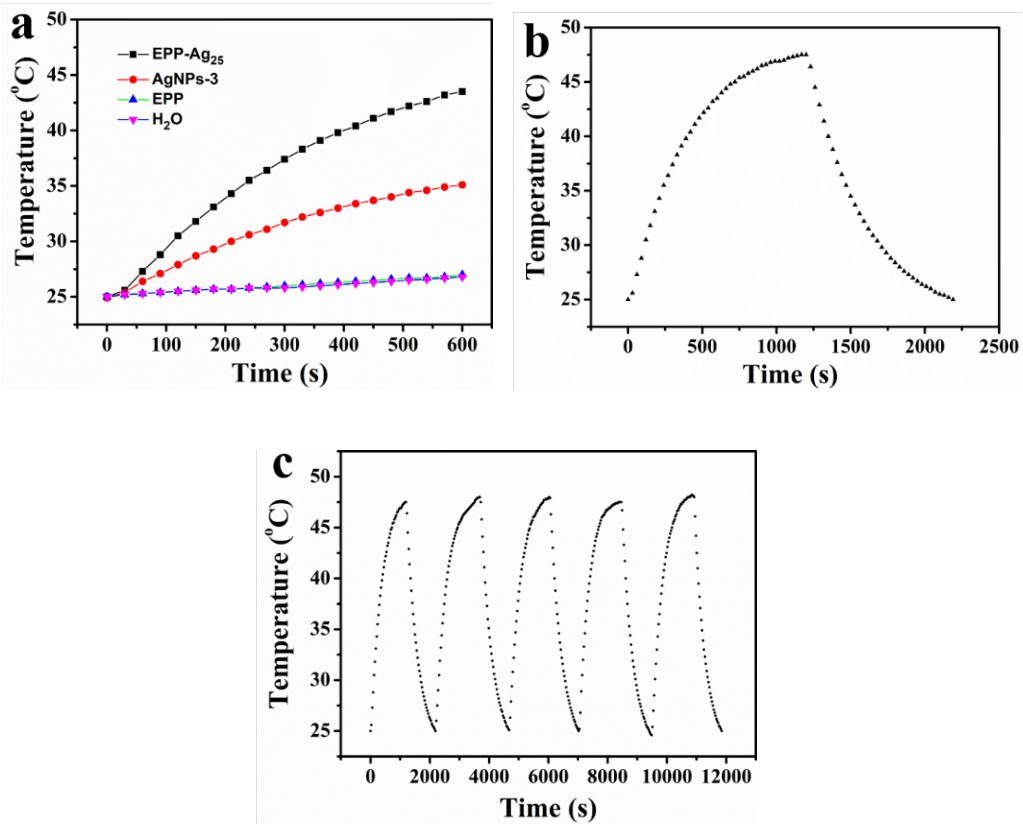

Fig. 7. (a) Temperature of EPP-Ag_{25} NPs, Ag NPs, EPP and water upon irradiation at 1.75 W/cm^2 for 600 s, (b) EPP-Ag_{25} NPs irradiated at 1.75 W/cm^2 to the highest temperature and cooled down naturally, (c) 5 heating and cooling cycles

3.5. Antibacterial performance

Bacteria were cultured in a 96-well plate, EPP-Ag_{25} NPs were added to test their antibacterial property. As shown in **Fig. 8**, EPP had no inhibitory effect on *Escherichia coli*. The inhibition rate of Ag NPs-3 prepared without EPP template increased with the concentration from 100 to 500 μg/mL, the maximum inhibition rate was 17% when the concentration of Ag NPs-3 was 500 μg/mL. Similarly, the inhibition rate of EPP-Ag_{25} NPs on *Escherichia coli* increased with the concentration from 100 to 500 μg/mL, and the inhibition rate raised from 54% to 68%. As for the EPP-Ag_{25} NPs + L group with irradiation by an 808 nm near-infrared laser, the inhibition rate of *Escherichia coli* increased from 60% to 71% Therefore, the antibacterial effect of EPP-Ag_{25} NPs was concentration-dependent, and the antibacterial effect became stronger after the addition of photothermal effect of EPP-Ag_{25} NPs.

EPP-Ag_{25} NPs possessed antibacterial properties and their antibacterial ability was

enhanced under photothermal conditions. The antibacterial properties of EPP-Ag_{25} NPs were provided by the stabilized Ag NPs. Ag NPs were ideal candidates for antimicrobial applications due to their broad-spectrum activity. The antibacterial mechanism of Ag NPs was based on the release of Ag^+ through delayed oxidation to achieve the antibacterial effect. Then, the released Ag^+ attached to the biofilm due to electrostatic attraction, causing the bacterial shell to rupture, thereby improving the permeability of the bacterial cell membrane. Finally, Ag NPs provided a better effect for antibacterial due to the release of reactive oxygen species after they entered the bacteria. In addition, Ag NPs achieved the effect of disrupting bacterial morphology and inducing bacterial death by inducing increased ATP consumption and inactivation of enzymes and proteins [43, 44]. The antibacterial properties of EPP-Ag_{25} NPs were improved under 808 nm laser irradiation. This was because *Escherichia coli* was heat-sensitive and died at 48-60°C. The photothermal properties of EPP-Ag_{25} NPs with unique morphologies enabled them to reach high temperature under 808 nm laser irradiation [45]. Therefore, EPP-Ag_{25} NPs had a good bacteriostatic effect on *Escherichia coli* based on the above-mentioned reasons.

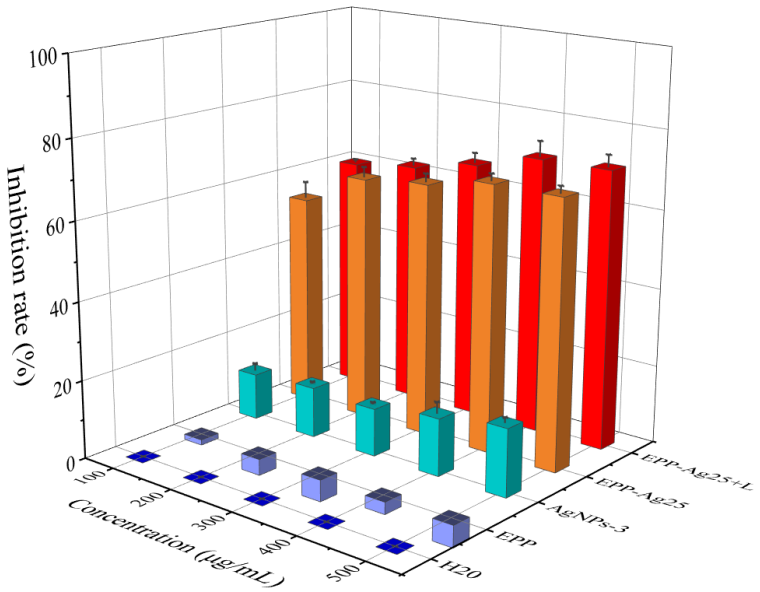

Fig. 8. Inhibition rate of EPP, Ag NPs-3, EPP-Ag_{25} NPs, EPP-Ag_{25} NPs + L to *Escherichia coli*

3.6. Cell viability

Biocompatibility was especially important for the use of nanomaterials in the biological

field. The MTT assay is a common method used to evaluate the cytotoxicity of nanomaterials [46]. Therefore, the MTT assay was used to assess the cytotoxicity of EPP-Ag_n NPs to HeLa cells. As shown in **Fig. 9(a, b, c)**, EPP and EPP-Ag_n NPs with different concentrations were co-incubated with HeLa cells, and it was found that when the concentration of EPP and EPP-Ag_n NPs (n = 10, 25, 40) was less than 100 g/mL, the cell viability was bigger than 90%. This result demonstrated that EPP and EPP-Ag_n NPs were biocompatible. This could be due to the negative charge on the surface of biocompatible EPP and EPP-Ag_n NPs, which reduced their interaction with cells. However, EPP-Ag_n NPs showed high cytotoxicity after the cells irradiated with an 808 nm near-infrared laser, indicating their antitumor ability. This should be due to the release of Ag^+ from EPP-Ag_{25} NPs and the photothermal effect of EPP-Ag_{25} NPs.

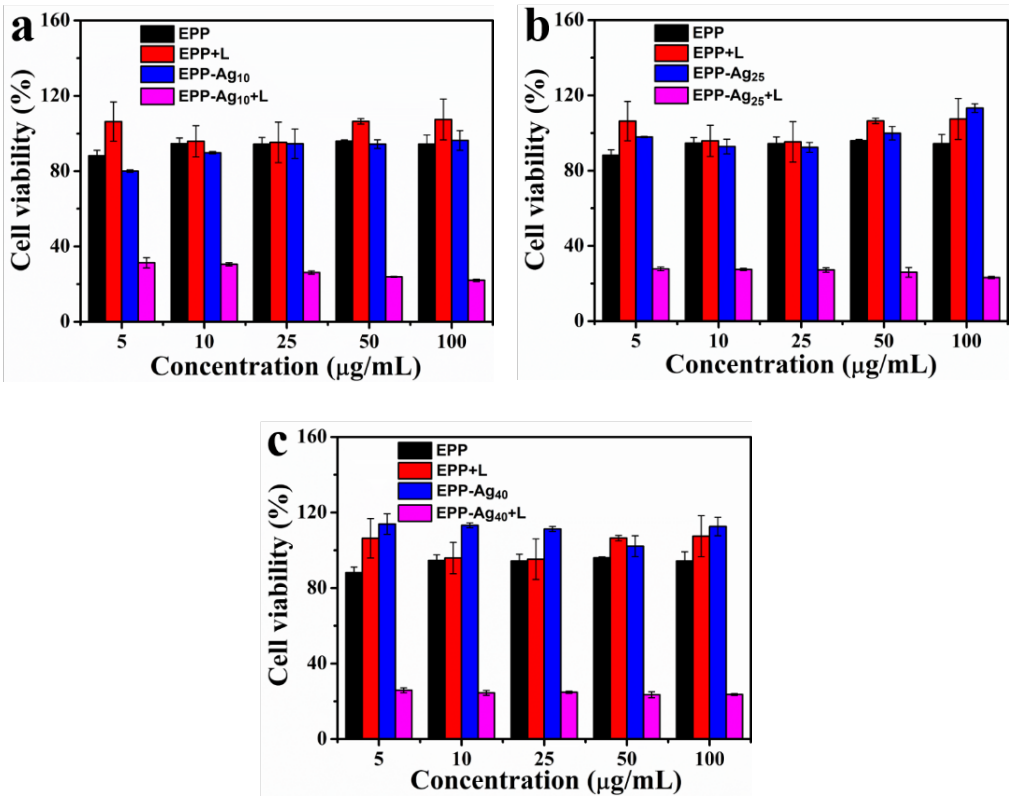

Fig. 9. Cell viabilities of HeLa cells treated with (a) EPP-Ag_{10} NPs, (b) EPP-Ag_{25} NPs and (c) EPP-Ag_{40} NPs

4. Conclusions

In conclusion, EPP was extracted and EPP-Ag_n NPs were prepared for the first time. EPP-Ag_n NPs had an irregular morphology and small size. They also had good

dispersibility and stability. As a result, they had high catalytic activity, and the conversion rate for organic pollutants 4-NP was as high as 94%. The k_{nor} and TOF (EPP-Ag_{25} NPs) were 1.67 s^{-1} mM^{-1} and 771.62 h^{-1}. Furthermore, EPP-Ag_n NPs demonstrated photothermal performance, and the photothermal conversion efficiency reached 22%. Finally, EPP-Ag_{25} NPs had an inhibition rate on *Escherichia coli* up to 68%. The inhibition rates on *Escherichia coli* of EPP-Ag_{25} NPs under photothermal effect reached 71%. MTT experiment demonstrated that EPP-Ag_n NPs had good biocompatibility and their photothermal antitumor effects were enhanced under 808 nm irradiation. Thus, EPP-Ag_n NPs have a wide range of applications in catalysis and biomedicine.

Acknowledgments

This research was funded by Natural Science Foundation of Hebei Province (B2017203229), Key Program of Hebei University of Environmental Engineering (2020ZRZD02), Youth Foundation Project supported by the Hebei Education Department of China (QN2022124), Talent Training Programs of Hebei Province (A201901068, A201901069), Scientific Research Key Projects of Education Department of Hebei Province (ZD2019024) and Science and Technology Support Program of Qinhuangdao (202101A007).

Conflicts of Interest:

The authors declare no conflict of interest.

AUTHOR INFORMATION

Corresponding Author

Notes hanzs@ysu.edu.cn, lgwang@ysu.edu.cn

References

[1] M.P. Sooraj, A.S. Nair, D. Vineetha, Sunlight-mediated green synthesis of silver nanoparticles using Sida retusa leaf extract and assessment of its antimicrobial and catalytic activities, Chem. Zvesti 75(1) (2020) 351-363.

[2] J. Wang, J. Zhang, K. Liu, J. He, Y. Zhang, S. Chen, G. Ma, Y. Cui, L. Wang, D. Gao, Synthesis of gold nanoflowers stabilized with amphiphilic daptomycin for enhanced photothermal antitumor and antibacterial effects, Int. J. Pharm. 580 (2020) 119231.

[3] S. Khorrami, A. Zarepour, A. Zarrabi, Green synthesis of silver nanoparticles at low temperature in a fast pace with unique DPPH radical scavenging and selective cytotoxicity against MCF-7 and BT-20 tumor cell lines, Biotechnol. Rep. 24 (2019) e00393.
[4] C. Wang, J. Yin, S. Han, T. Jiao, Z. Bai, J. Zhou, L. Zhang, Q. Peng, Preparation of palladium nanoparticles decorated polyethyleneimine/polycaprolactone composite fibers constructed by electrospinning with highly efficient and recyclable catalytic performances, Catalysts 9(6) (2019) 559.
[5] K. Iqbal, A. Iqbal, A.M. Kirillov, C. Shan, W. Liu, Y. Tang, A new multicomponent CDs/Ag@Mg–Al–Ce-LDH nanocatalyst for highly efficient degradation of organic water pollutants, J. Mater. Chem. A 6(10) (2018) 4515-4524.
[6] M. Aravind, A. Ahmad, I. Ahmad, M. Amalanathan, K. Naseem, S.M.M. Mary, C. Parvathiraja, S. Hussain, T.S. Algarni, M. Pervaiz, M. Zuber, Critical green routing synthesis of silver NPs using jasmine flower extract for biological activities and photocatalytical degradation of methylene blue, J. Environ. Chem. Eng. 9(1) (2021) 104877.
[7] S. Marimuthu, A.J. Antonisamy, S. Malayandi, K. Rajendran, P.-C. Tsai, A. Pugazhendhi, V.K. Ponnusamy, Silver nanoparticles in dye effluent treatment: A review on synthesis, treatment methods, mechanisms, photocatalytic degradation, toxic effects and mitigation of toxicity, J. Photochem. Photobiol., B 205 (2020) 111823.
[8] V. Seerangaraj, S. Sathiyavimal, S.N. Shankar, J.G.T. Nandagopal, P. Balashanmugam, F.A. Al-Misned, M. Shanmugavel, P. Senthilkumar, A. Pugazhendhi, Cytotoxic effects of silver nanoparticles on Ruellia tuberosa: Photocatalytic degradation properties against crystal violet and coomassie brilliant blue, J. Environ. Chem. Eng. 9(2) (2021) 105088.
[9] M.P. Desai, R.V. Patil, K.D. Pawar, Green biogenic approach to optimized biosynthesis of noble metal nanoparticles with potential catalytic, antioxidant and antihaemolytic activities, Process Biochem. 98 (2020) 172-182.
[10] T.A. Jorge de Souza, L.R. Rosa Souza, L.P. Franchi, Silver nanoparticles: An integrated view of green synthesis methods, transformation in the environment, and toxicity, Ecotoxicol. Environ. Saf. 171 (2019) 691-700.
[11] A. Khatua, E. Priyadarshini, P. Rajamani, A. Patel, J. Kumar, A. Naik, M. Saravanan, H. Barabadi, A. Prasad, l. Ghosh, B. Paul, R. Meena, Phytosynthesis, characterization and fungicidal potential of emerging gold nanoparticles using pongamia pinnata leave extract: A novel approach in nanoparticle synthesis, J. Cluster Sci. 31(1) (2019) 125-131.
[12] P.G. Jamkhande, N.W. Ghule, A.H. Bamer, M.G. Kalaskar, Metal nanoparticles synthesis: An overview on methods of preparation, advantages and disadvantages, and applications, J. Drug Delivery Sci. Technol. 53 (2019) 101174.
[13] A. Desireddy, B.E. Conn, J. Guo, B. Yoon, R.N. Barnett, B.M. Monahan, K. Kirschbaum, W.P. Griffith, R.L. Whetten, U. Landman, T.P. Bigioni, Ultrastable silver nanoparticles, Nature 501(7467) (2013) 399-402.
[14] D. Cassano, M. Santi, F. D'Autilia, A.K. Mapanao, S. Luin, V. Voliani, Photothermal effect by NIR-responsive excretable ultrasmall-in-nano architectures,

Mater. Horiz. 6(3) (2019) 531-537.
[15] A.J. Young, C. Eisen, G.M.D.M. Rubio, J.M. Chin, M.R. Reithofer, pH responsive histidin-2-ylidene stabilized gold nanoparticles, J. Inorg. Biochem. 199 (2019) 110707.
[16] M. Mahiuddin, P. Saha, B. Ochiai, Green synthesis and catalytic activity of silver nanoparticles based on piper chaba stem eextracts, Nanomaterials 10(9) (2020) 1777.
[17] L. Fan, X. Ji, G. Lin, K. Liu, S. Chen, G. Ma, W. Xue, X. Zhang, L. Wang, Green synthesis of stable platinum nanoclusters with enhanced peroxidase-like activity for sensitive detection of glucose and glutathione, Microchem. J. 166 (2021) 106202.
[18] Y. Liang, H. Li, L. Fan, R. Li, Y. Cui, X. Ji, H. Xiao, J. Hu, L. Wang, Zwitterionic daptomycin stabilized palladium nanoparticles with enhanced peroxidase-like properties for glucose detection, Colloids Surf., A 633 (2022) 127797.
[19] Y.A. Selim, M.A. Azb, I. Ragab, M. H. M. Abd El-Azim, Green synthesis of zinc oxide nanoparticles using aqueous extract of deverra tortuosa and their cytotoxic activities, Sci. Rep. 10(1) (2020) 3445.
[20] M. Behravan, A. Hossein Panahi, A. Naghizadeh, M. Ziaee, R. Mahdavi, A. Mirzapour, Facile green synthesis of silver nanoparticles using Berberis vulgaris leaf and root aqueous extract and its antibacterial activity, Int. J. Biol. Macromol. 124 (2019) 148-154.
[21] R. Li, Z. Xia, B. Li, Y. Tian, G. Zhang, M. Li, J. Dong, Advances in supercritical carbon dioxide extraction of bioactive substances from different parts of ginkgo biloba L, Molecules 26(13) (2021) 4011.
[22] Z. Zhang, S. Chen, H. Mei, J. Xuan, X. Guo, L. Couch, V.N. Dobrovolsky, L. Guo, N. Mei, Ginkgo biloba leaf extract induces DNA damage by inhibiting topoisomerase II activity in human hepatic cells, Sci. Rep. 5(1) (2015) 14633.
[23] X. Yan, W. Wang, M. Liu, Z. Zhao, Preparation of oligosaccharides by degradation of polysaccharides from chinese jujube and its biological activity, Int. J. Polym. Sci. 2018 (2018) 1-8.
[24] L. Dong, R. Li, L. Wang, X. Lan, H. Sun, Y. Zhao, L. Wang, Green synthesis of platinum nanoclusters using lentinan for sensitively colorimetric detection of glucose, Int. J. Biol. Macromol. 172 (2021) 289-298.
[25] T. Cui, S. Li, S. Chen, Y. Liang, H. Sun, L. Wang, “Stealth” dendrimers with encapsulation of indocyanine green for photothermal and photodynamic therapy of cancer, Int. J. Pharm. 600 (2021) 120502.
[26] Y. Su, L. Li, Structural characterization and antioxidant activity of polysaccharide from four auriculariales, Carbohydr. Polym. 229 (2020) 115407.
[27] M.E. Taghavizadeh Yazdi, A. Hamidi, M.S. Amiri, R. Kazemi Oskuee, H.A. Hosseini, A. Hashemzadeh, M. Darroudi, Eco-friendly and plant-based synthesis of silver nanoparticles using Allium giganteum and investigation of its bactericidal, cytotoxicity, and photocatalytic effects, J. Mater. Sci. Technol. 34(8) (2019) 490-497.
[28] J. He, J. Wang, S. Gao, Y. Cui, X. Ji, X. Zhang, L. Wang, Biomineralized synthesis of palladium nanoflowers for photothermal treatment of cancer and wound healing, Int. J. Pharm. 615 (2022) 121489-121489.
[29] A. Kaur, S. Preet, V. Kumar, R. Kumar, R. Kumar, Synergetic effect of vancomycin loaded silver nanoparticles for enhanced antibacterial activity, Colloids Surf., B 176

(2019) 62-69.
[30] P. Attri, S. Garg, J.K. Ratan, A.S. Giri, Silver nanoparticles from Tabernaemontana divaricate leaf extract: mechanism of action and bio-application for photo degradation of 4-aminopyridine, Environ. Sci. Pollut. Res. (2022).
[31] M. S. J. Khan, T. Kamal, F. Ali, A. M. Asiri, S. B. Khan, Chitosan-coated polyurethane sponge supported metal nanoparticles for catalytic reduction of organic pollutants. Int. J. Biol. Macromol. 132 (2019) 772-783.
[32] L. Qin, H. Yi, G. Zeng, C. Lai, D. Huang, P. Xu, Y. Fu, J. He, B. Li, C. Zhang, M. Cheng, H. Wang, X. Liu, Hierarchical porous carbon material restricted Au catalyst for highly catalytic reduction of nitroaromatics, J. Hazard. Mater. 380 (2019) 120864.
[33] S. A. Khan, N. Khan, U. Irum, A. Farooq, A. M. Asiri, E. M. Bakhsh, S. B. Khan, Cellulose acetate-Ce/Zr@Cu-0 catalyst for the degradation of organic pollutant. Int. J. Biol. Macromol. 153 (2020) 806-816.
[34] F. Liu, X. Liu, F. Chen, Q. Fu, Tannic Acid: A green and efficient stabilizer of Au, Ag, Cu and Pd nanoparticles for the 4-Nitrophenol reduction, Suzuki–Miyaura coupling reactions and click reactions in aqueous solution, J. Colloid Interface Sci. 604 (2021) 281-291.
[35] Z. Yan, L. Fu, X. Zuo, H. Yang, Green assembly of stable and uniform silver nanoparticles on 2D silica nanosheets for catalytic reduction of 4-nitrophenol, Appl. Catal., B 226 (2018) 23-30.
[36] M. Li, L. Huang, X. Wang, Z. Song, W. Zhao, Y. Wang, J. Liu, Direct generation of Ag nanoclusters on reduced graphene oxide nanosheets for efficient catalysis, antibacteria and photothermal anticancer applications, J. Colloid Interface Sci. 529 (2018) 444-451.
[37] Y. Wang, P. Gao, Y. Wei, Y. Jin, S. Sun, Z. Wang, Y. Jiang, Silver nanoparticles decorated magnetic polymer composites (Fe_3O_4@PS@Ag) as highly efficient reusable catalyst for the degradation of 4-nitrophenol and organic dyes, J. Environ. Manage. 278 (2021) 111473.
[38] D. Parida, E. Moreau, R. Nazir, K.A. Salmeia, R. Frison, R. Zhao, S. Lehner, M. Jovic, S. Gaan, Smart hydrogel-microsphere embedded silver nanoparticle catalyst with high activity and selectivity for the reduction of 4-nitrophenol and azo dyes, J. Hazard. Mater. 416 (2021) 126237.
[39] H.-L. Cao, C. Liu, F.-Y. Cai, X.-X. Qiao, A.B. Dichiara, C. Tian, J. Lü, In situ immobilization of ultra-fine Ag NPs onto magnetic Ag@RF@Fe_3O_4 core-satellite nanocomposites for the rapid catalytic reduction of nitrophenols, Water Res. 179 (2020) 115882.
[40] T.K. Das, S. Remanan, S. Ghosh, N.C. Das, An environment friendly free-standing cellulose membrane derived for catalytic reduction of 4-nitrophenol: A sustainable approach, J. Environ. Chem. Eng. 9(1) (2021) 104596.
[41] C. Fang, P. Yan, Z. Ren, Y. Wang, X. Cai, X. Li, G. Han, Multifunctional MoO_2-ICG nanoplatform for 808nm-mediated synergetic photodynamic/photothermal therapy, Appl. Mater. Today 15 (2019) 472-481.
[42] S. Yu, J. Zhang, S. Liu, Z. Ma, H. Sun, Z. Liu, L. Wang, Self-assembly synthesis of flower-like gold nanoparticles for photothermal treatment of cancer, Colloids Surf.,

A 647 (2022) 129163.
[43] S. Duan, R. Wu, Y.-H. Xiong, H.-M. Ren, C. Lei, Y.-Q. Zhao, X.-Y. Zhang, F.-J. Xu, Multifunctional antimicrobial materials: From rational design to biomedical applications, Prog. Mater. Sci. 125 (2022) 100887.
[44] M.-M. Zaharia, C.-A. Ghiorghita, M.-A. Trofin, F. Doroftei, I. Rosca, M. Mihai, Multifunctional composites of zwitterionic resins and silver nanoparticles for point-of-demand antimicrobial applications, Mater. Chem. Phys. 275 (2022) 125225.
[45] X. Xu, M. Fan, Z. Yu, Y. Zhao, H. Zhang, J. Wang, M. Wu, F. Sun, X. Xu, C. Ding, J. Li, A removable photothermal antibacterial “warm paste” target for cariogenic bacteria, Chem. Eng. J. 429 (2022) 132491.
[46] H. Adeli, M.T. Khorasani, M. Parvazinia, Wound dressing based on electrospun PVA/chitosan/starch nanofibrous mats: Fabrication, antibacterial and cytocompatibility evaluation and in vitro healing assay, Int. J. Biol. Macromol. 122 (2019) 238-254.